Supplement of Atmos. Chem. Phys., 26, 5169–5184, 2026
https://doi.org/10.5194/acp-26-5169-2026-supplement

Atmospheric Chemistry and Physics
Open Access
EGU

Supplement of

Distinct drivers of recent seasonal precipitation increase over Central Asia: roles of anthropogenic aerosols and greenhouse gases

Jianing Guo et al.

Correspondence to: Xiaoning Xie (xnxie@ieecas.cn)

This PDF file includes:

Tables S1 to S3

Figures. S1 to S13

References

Table S1. Detailed information on the PDRMIP models used in this study. Table adapted from Myhre et al. (2017)

Model	Version	Resolution	Ocean setup	Baseline	Aerosol emissions	Aerosol processes
CanESM2	2010	2.8° × 2.8°, 35 levels	Coupled ocean	Year 2000	Emissions	Full microphysics for aerosol-cloud interactions
GISS-E2-R	E2-R	2° × 2.5°, 40 le vels	Coupled ocean	Year 2000	Fixed concentrations	No aerosol microphysics effects
HadGEM2	6.6.3	1.875°×1.25°, 38 levels	Coupled ocean	Year 1860	Emissions	Full microphysics for aerosol-cloud interactions
HadGEM3	3	1.875° × 1.25°, 85 levels	Coupled ocean	Year 2000	Fixed concentrations	Microphysics for aerosol-cloud interactions (not for BC and dust)
IPSL-CM5A	5A	3.75° × 1.875°, 39 levels	Coupled ocean	Year 2000	Fixed concentrations	Aerosol microphysics for Twomey effect included
MIROC-SPRIN TARS	5.9.0	1.4° × 1.4°, 40 levels	Coupled ocean	Year 2000	Emissions	Full microphysics for aerosol-cloud interactions
NCAR-CESM1-CAM4	1.0.3	2.5° × 1.9°, 26 levels	Slab ocean	Year 2000	Fixed concentrations	No aerosol microphysics effects
NCAR-CESM1-CAM5	1.1.2	2.5° × 1.9°, 30 levels	Coupled ocean	Year 2000	Emissions	Full aerosol microphysics
NorESM1	1-M	2.5° × 1.9°, 26 levels	Coupled ocean	Year 2000	Fixed concentrations	Microphysics of aerosol-cloud interactions included through prescribed cloud condensation nuclei

Table S2. Simulated scenario of the PDRMIP models used in this study.

Simulated scenario	CanESM2	GISS-E2-R	HadGEM2	HadGEM3	IPSL-CM5A	MIROC-SPRINTARS	NCAR-CESM1-CAM4	NCAR-CESM1-CAM5	NorESM1
CO_2x2	√	√	√	√	√	√	√	√	√
CH_4x3	√	√	√	√	√	√	√	√	√
Solar+2%	√	√	√	√	√	√	√	√	√
Sulx10Asia		√		√	√	√	√	√	√
BCx10Asia		√		√	√	√		√	√

* Ticks indicate the models used in the different simulation scenarios.

Table S3. Information of the DAMIP and ScenarioMIP models in CMIP6 employed in this study.

Model	Institution/Country	Resolution (Longitude × Latitude)	DAMIP models				ScenarioMIP models
			historical	hist-GHG	hist-aer	hist-nat	
ACCESS-CM2	CSIRO/Australian	192 × 144	√	√	√	√	√
ACCESS-ESM1-5	CSIRO/Australian	192 × 145	√(40)	√	√	√	√(40)
BCC-CSM2-MR	BCC/China	320 × 160	√	√	√	√	
CanESM5	CCCma/Canada	128 × 64	√	√	√	√	√(25)
CESM2	NCAR/USA	288 × 192	√	√	√	√	√
CMCC-CM2-SR5	CMCC/Italia	288 × 192	√				
CNRM-CM6-1	CNRM-CERFACS/France	256 × 128	√	√	√	√	√
CNRM-ESM2-1	CNRM-CERFACS/France	256 × 128					√
E3SM-2-0	LLNL/USA	360 × 180	√	√	√	√	
EC-Earth3	EC-Earth-Consortium/EU	512 × 256	√				√
FGOALS-g3	CAS/China	180 × 80	√				
GFDL-ESM4	NOAA-GFDL/USA	288 × 180	√	√	√	√	√
GISS-E2-1-G	GISS/USA	144 × 90	√				
HadGEM3-GC31-LL	MOHC/UK	192 × 144	√	√	√	√	
INM-CM5-0	INM/Russia	180 × 120	√				√
IPSL-CM6A-LR	IPSL/France	144 × 143	√	√	√	√	√
MIROC6	MIROC/Japan	256 × 128	√(50)	√	√	√	√(50)
MPI-ESM1-2-HR	MPI-M/Germany	384 × 192					√
MPI-ESM1-2-LR	MPI-M/Germany	192 × 96					√(30)
MRI-ESM2-0	MRI/Japan	320 × 160	√	√	√	√	
NorESM2-MM	NCC/Norway	288 × 192	√				√
UKESM1-0-LL	MOHC/UK	192 × 144					√

* The number in the bracket represents the ensemble members used in this study. All the other models used a single member. Ticks indicate the models used in the different analyses. Note that the NorESM2-MM is a different version compared to NorESM1 used in PDRMIP (Seland et al., 2020).

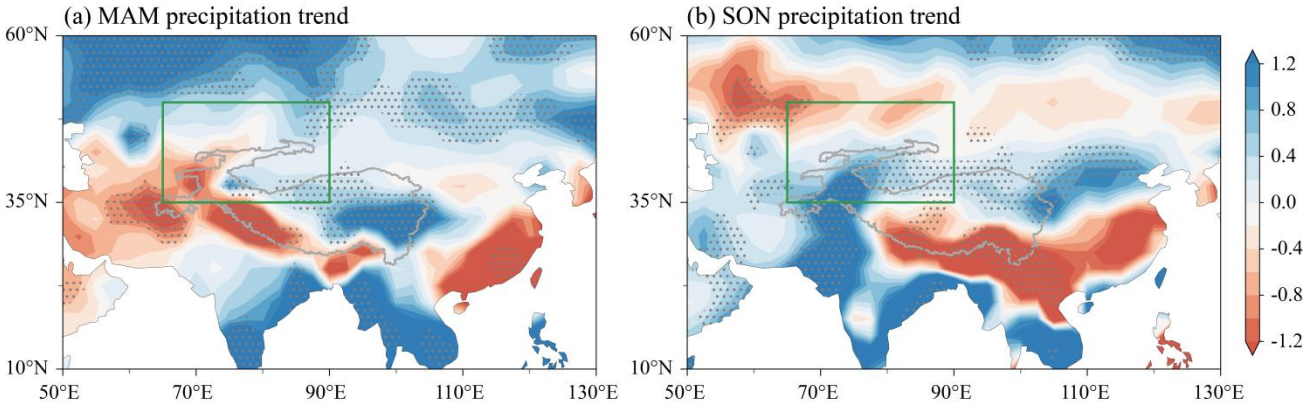

Figure S1. Spatial distributions of precipitation trends over Central Asia. (**a**) Spring (March–May, MAM) and (**b**) autumn (September–November, SON) precipitation trends (mm day^{-1} per 100 years) derived from GPCP during 1979–2014. The region of Central Asia (35°N–50°N, 65°E–90°E) is delineated by thick green boxes. The stippling indicates trends that are statistically significant at the 90% confidence level based on a standard *t*-test. The thick gray curves denote Tibetan Plateau terrain height > 2500 m.

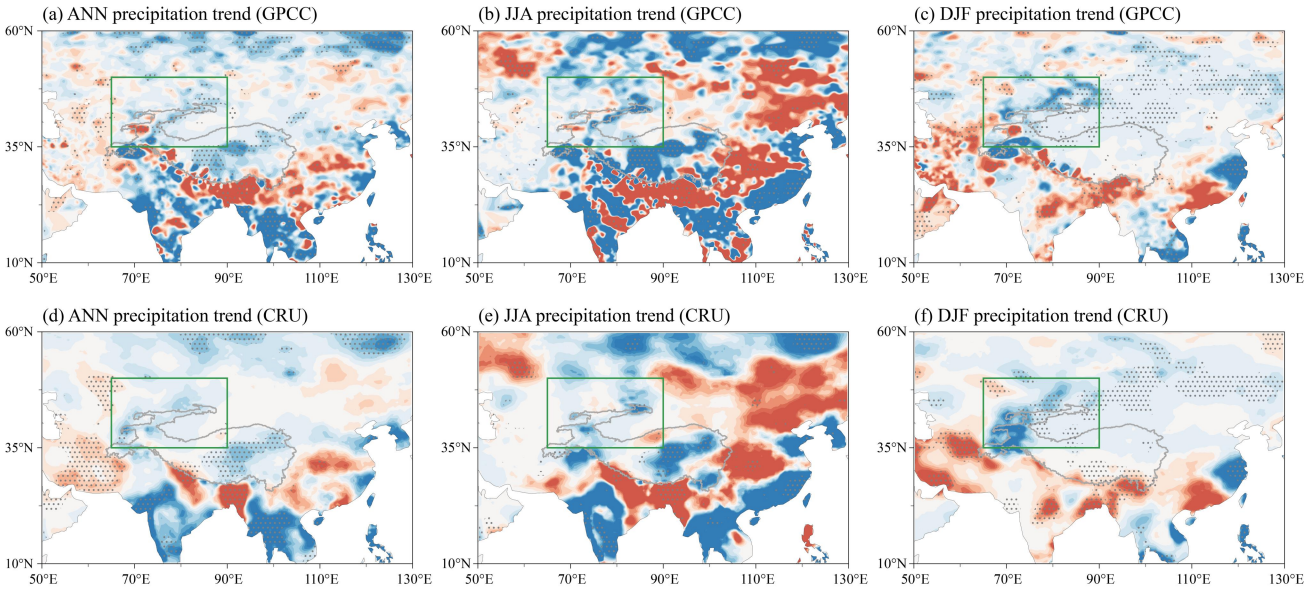

Figure S2. Spatial distributions of precipitation trends over Central Asia. (**a**) Annual (January–December, ANN), (**b**) summer (June–August, JJA), and (**c**) winter (December–February, DJF) precipitation trends (mm day^{-1} per 100 years) derived from GPCC during 1979–2014. (**d–f**) Same as (**a–c**), but derived from CRU. The region of Central Asia (35°N–50°N, 65°E–90°E) is delineated by thick green boxes. The stippling indicates trends that are statistically significant at the 90% confidence level based on a standard *t*-test. The thick gray curves denote Tibetan Plateau terrain height > 2500 m.

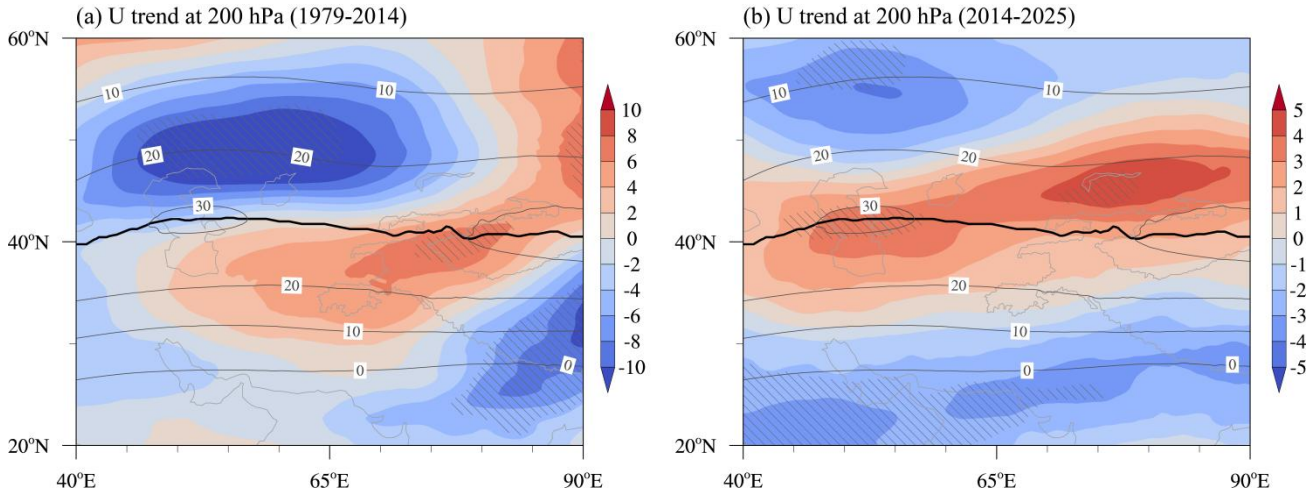

Figure S3. Spatial distributions of JJA zonal wind trends. **(a)** 1979–2014 (m s^{-1} per 100 years). **(b)** 2014–2025 (m s^{-1} per decade). The dark gray curves represent the climatological zonal wind and the thick black line denotes the westerly jet axis for 1979–2014. The slanted lines indicate trends that are statistically significant at the 90% confidence level based on a standard *t*-test.

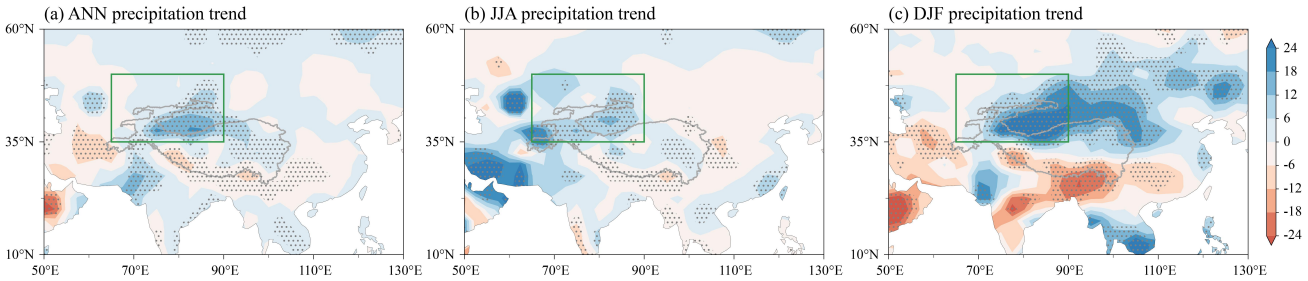

Figure S4. Spatial distributions of precipitation trends over Central Asia derived from GPCP. (**a**) Annual (January–December, ANN), (**b**) summer (June–August, JJA), and (**c**) winter (December–February, DJF) precipitation trends (% decade^{-1}) for 1979–2014, relative to the 1979–1998 seasonal mean. The region of Central Asia (35°N–50°N, 65°E–90°E) is delineated by thick green boxes. The stippling indicates trends that are statistically significant at the 90% confidence level based on a standard *t*-test. The thick gray curves denote Tibetan Plateau terrain height > 2500 m.

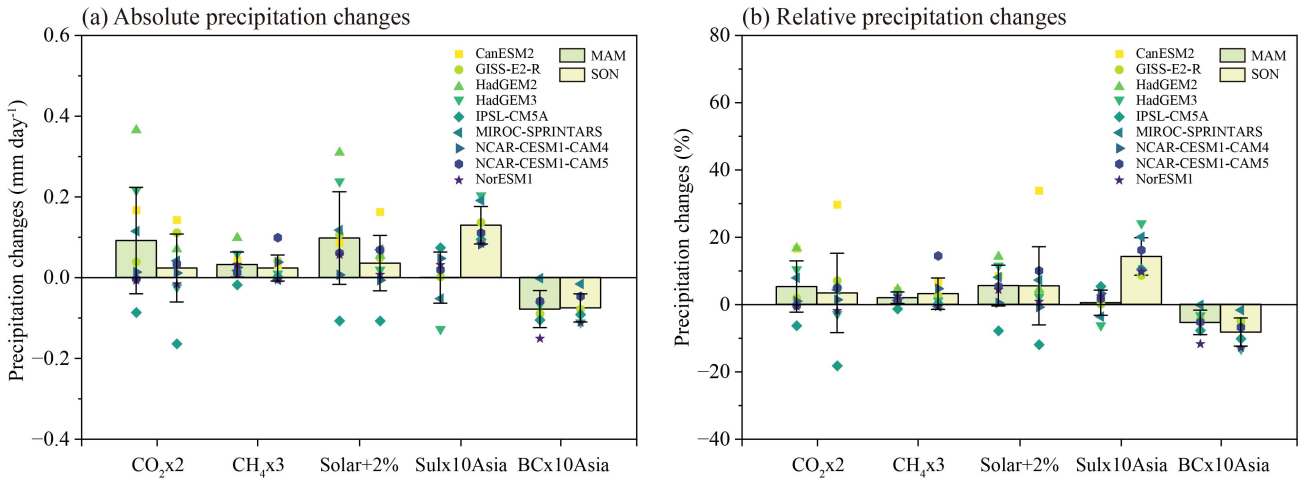

Figure S5. MAM and SON precipitation responses to CO_2x2, CH_4x3, Solar+2%, Sulx10Asia, and BCx10Asia forcings over Central Asia in PDRMIP. (**a**) Absolute changes in precipitation (mm day^{-1}) over Central Asia. (**b**) Relative changes in precipitation (%) over Central Asia. Error bars represent the multi-model ensemble standard deviation of PDRMIP.

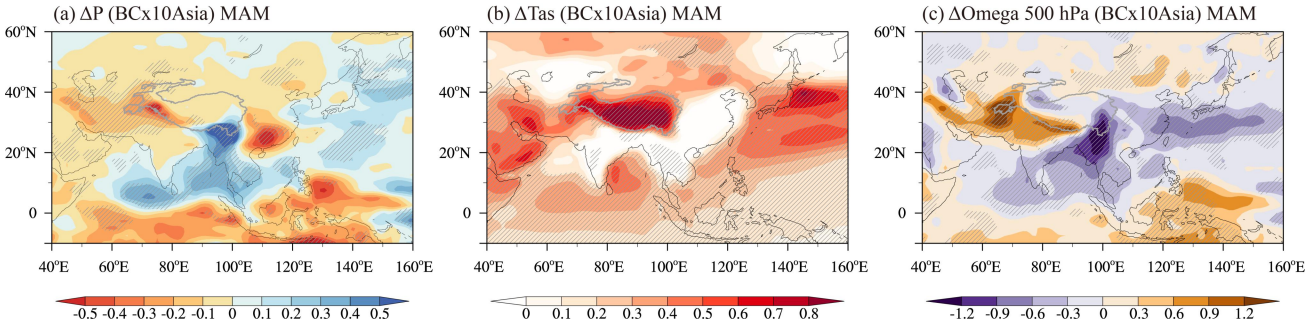

Figure S6. Multi-model mean anomalies during MAM induced by BCx10Asia forcing in PDRMIP. (**a**) Spatial distribution of changes in precipitation (mm day^{-1}), (**b**) near surface temperature (ΔTas, °C), and (**c**) 500 hPa vertical velocity (ΔOmega, 10^{-2} Pa s^{-1}) under BCx10Asia forcing. The slanted lines indicate where the multi-model mean of the PDRMIP models exceeds 1 standard deviation from zero. The thick gray curves denote Tibetan Plateau terrain height > 2500 m.

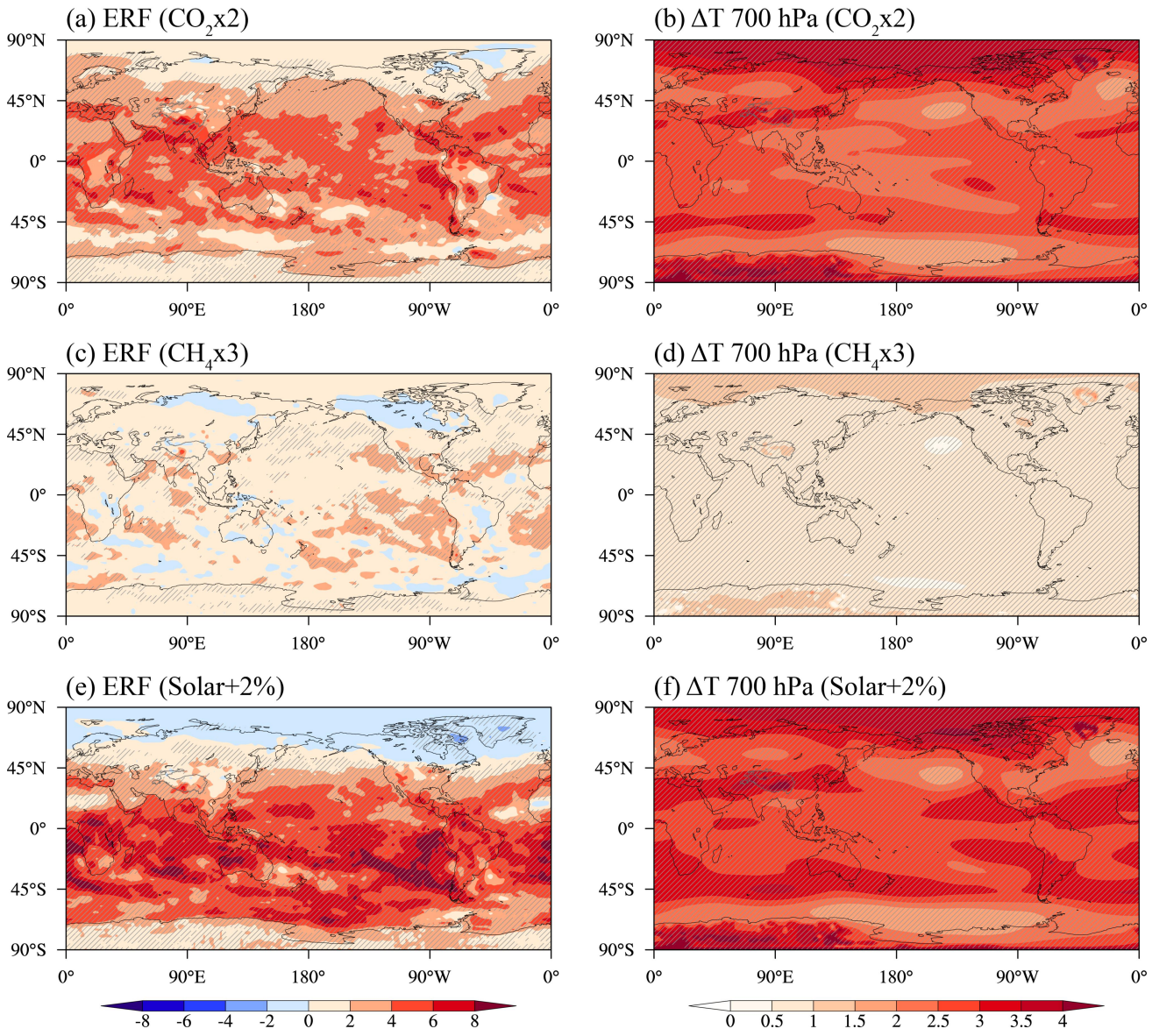

Figure S7. DJF effective radiative forcing and temperature changes induced by CO_2x2, CH_4x3, and Solar+2% in PDRMIP. Spatial distributions of (**a**) effective radiative forcing (ERF, W m^{-2}) and (**b**) temperature changes (ΔT, °C) at 700 hPa under CO_2x2 forcing. (**c, d**) Same as (**a, b**), but for CH_4x3 forcing. (**e, f**) Same as (**a, b**), but for Solar+2% forcing. The slanted lines indicate where the multi-model mean of the PDRMIP models exceeds 1 standard deviation from zero. The thick gray curves denote Tibetan Plateau terrain height > 2500 m.

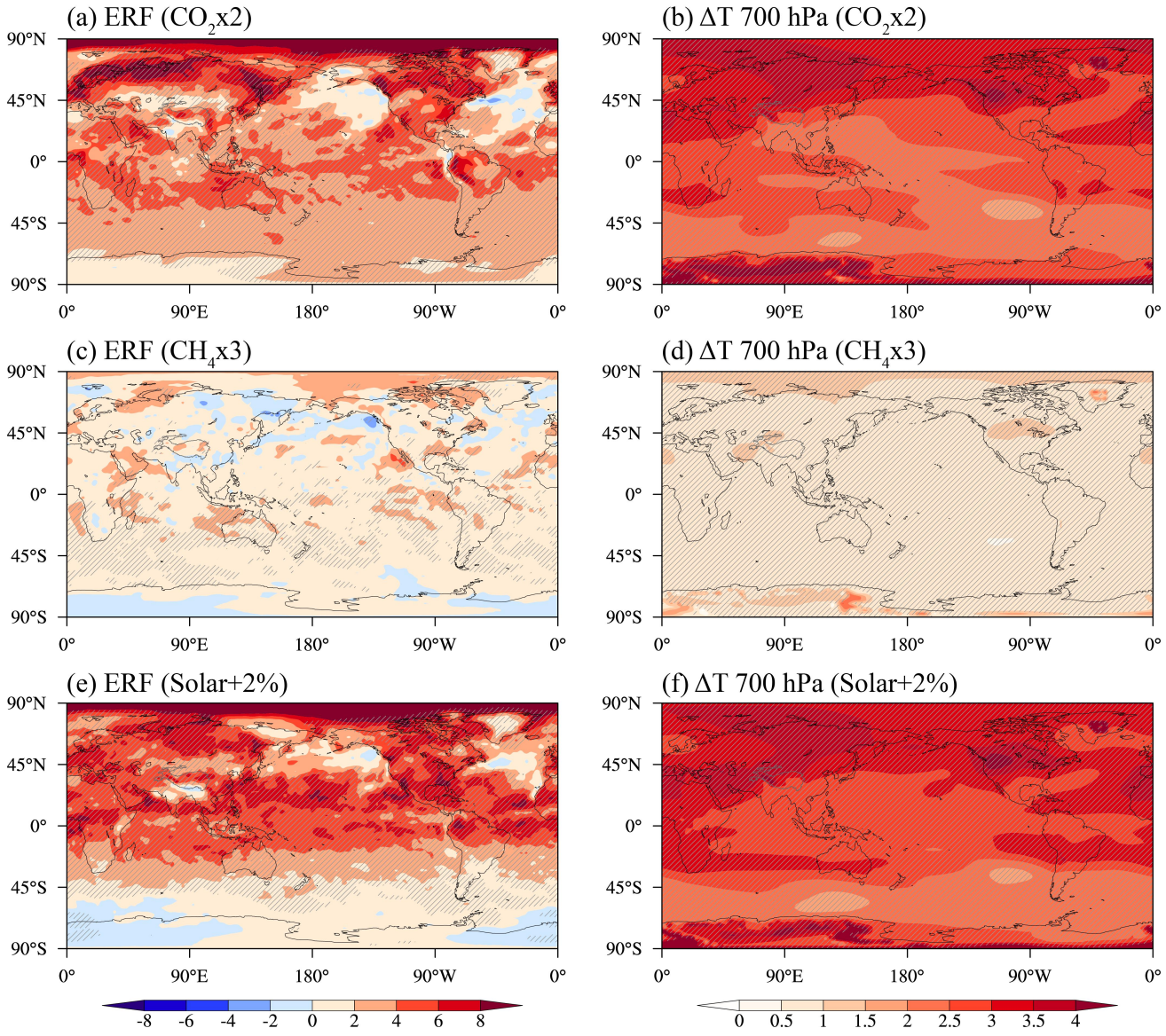

Figure S8. JJA effective radiative forcing and temperature changes induced by CO_2x2, CH_4x3, and Solar+2% in PDRMIP. Spatial distributions of (**a**) effective radiative forcing (ERF, W m^{-2}) and (**b**) temperature changes (ΔT, °C) at 700 hPa under CO_2x2 forcing. (**c, d**) Same as (**a, b**), but for CH_4x3 forcing. (**e, f**) Same as (**a, b**), but for Solar+2% forcing. The slanted lines indicate where the multi-model mean of the PDRMIP models exceeds 1 standard deviation from zero. The thick gray curves denote Tibetan Plateau terrain height > 2500 m.

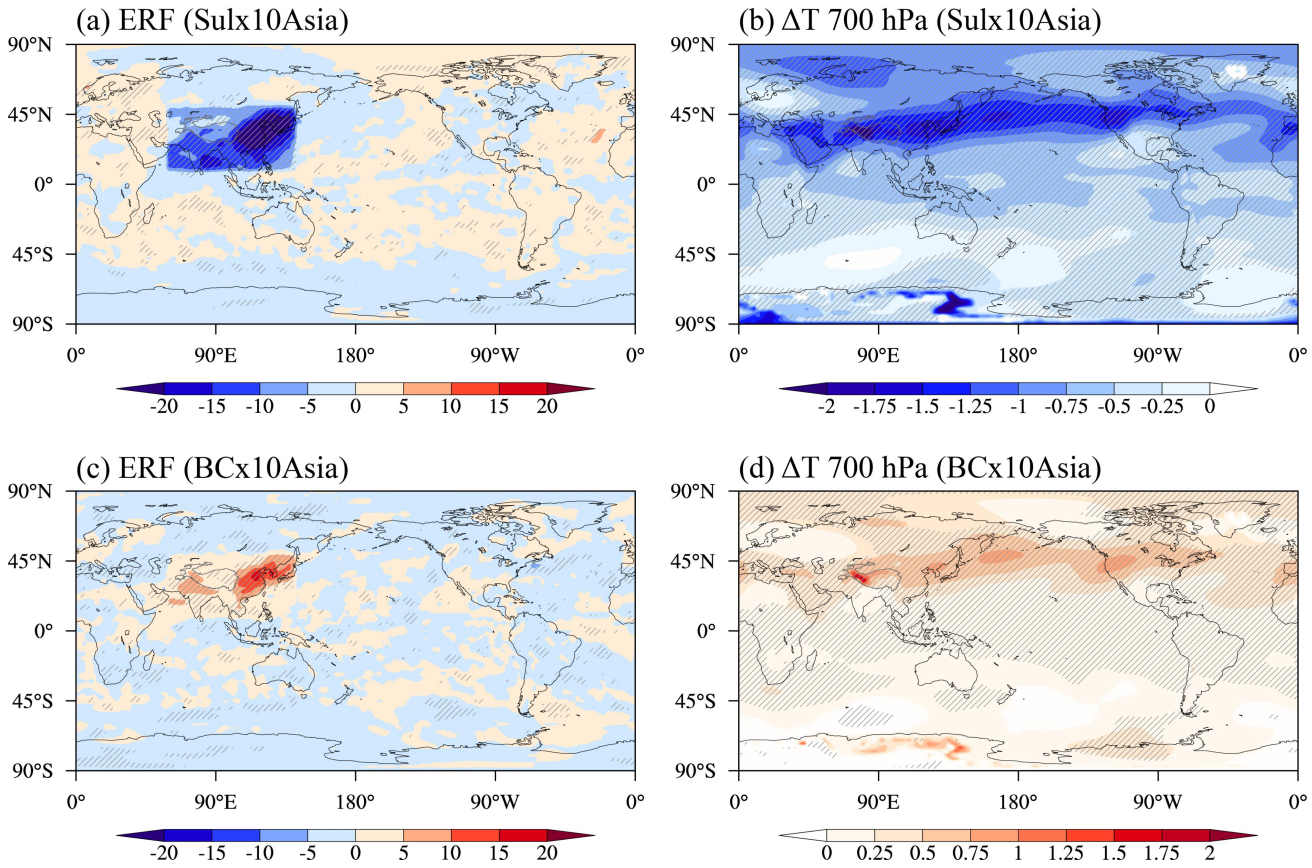

Figure S9. JJA effective radiative forcing and temperature changes induced by Sulx10Asia and BCx10Asia forcings in PDRMIP. Spatial distributions of (**a**) effective radiative forcing (ERF, W m^{-2}) and (**b**) temperature changes (ΔT, °C) at 700 hPa under Sulx10Asia forcing. (**c, d**) Same as (**a, b**), but for BCx10Asia forcing. The slanted lines indicate where the multi-model mean of the PDRMIP models exceeds 1 standard deviation from zero. The thick gray curves denote Tibetan Plateau terrain height > 2500 m.

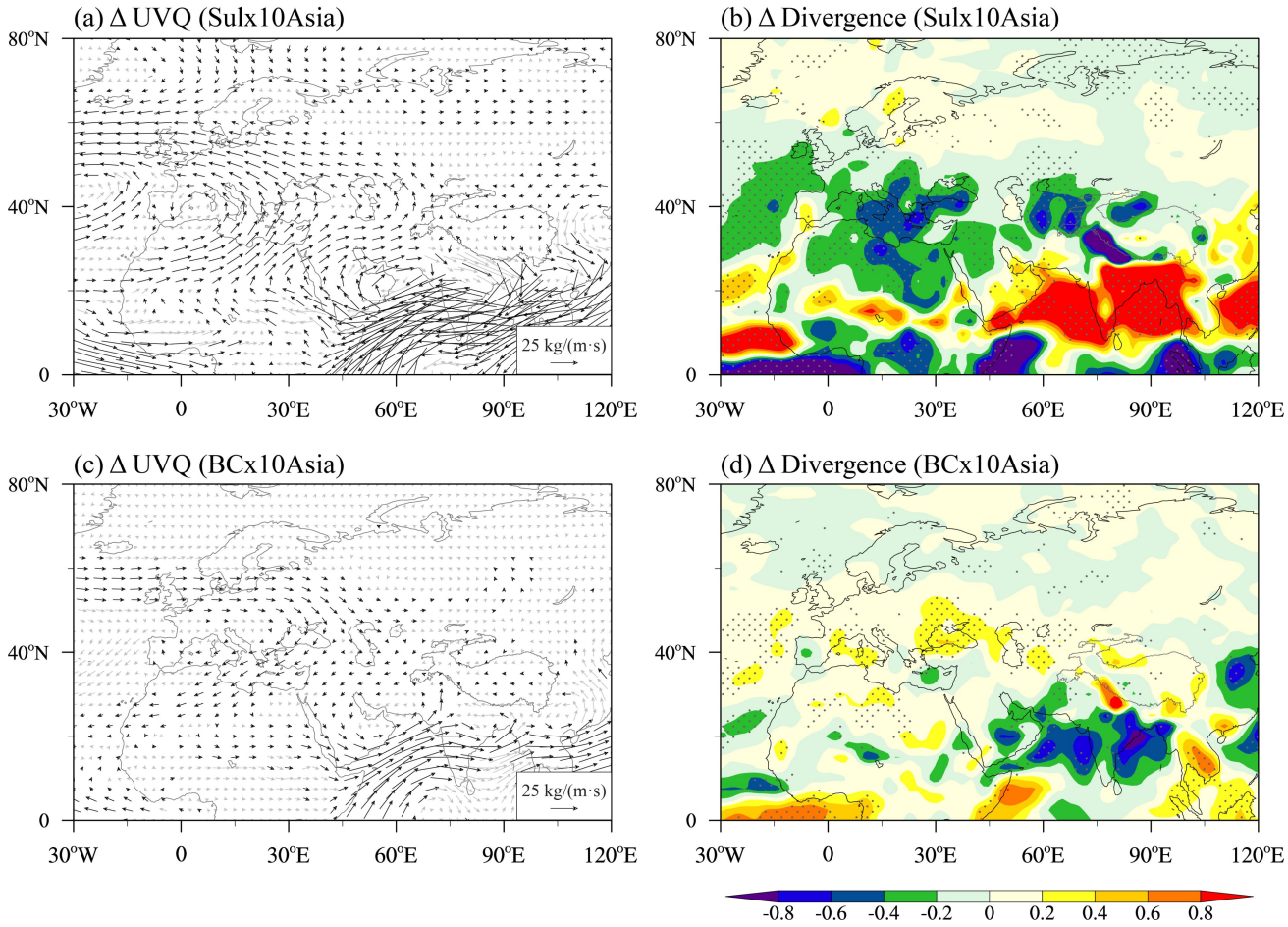

Figure S10. Multi-model mean JJA anomalies induced by Sulx10Asia and BCx10Asia forcings in PDRMIP. **(a)** Changes in vertically integrated (surface–300 hPa) moisture flux (Δ UVQ, kg m^{-1} s^{-1}) and **(b)** moisture divergence (Δ Divergence 10^{-5} kg m^{-2} s^{-1}) under Sulx10Asia forcing. (**c, d**) Same as (**a, b**), but for BCx10Asia forcing. Black arrows in **(b, d)** and gray stippled regions in **(a, c)** indicate where the PDRMIP multi-model mean changes exceed 1 standard deviation from zero.

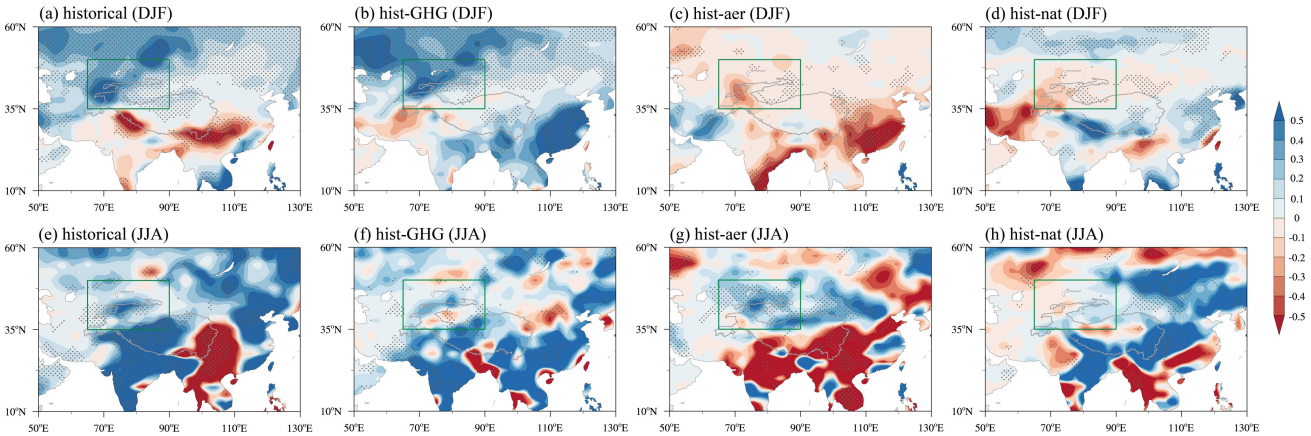

Figure S11. Spatial distributions of seasonal precipitation trends in DAMIP. Spatial distribution of DJF Central Asian precipitation trend (mm day^{-1} per 100 years) for (**a**) historical, (**b**) hist-GHG, (**c**) hist-aer, and (**d**) hist-nat simulations during 1979–2014. (**e**–**h**) Same as (**a**–**d**) but for JJA precipitation trends. Central Asia is outlined by thick green boxes, and gray stippling indicates regions where at least 70% of the models have the same sign of trend. Thick gray curves denote Tibetan Plateau terrain height > 2500 m.

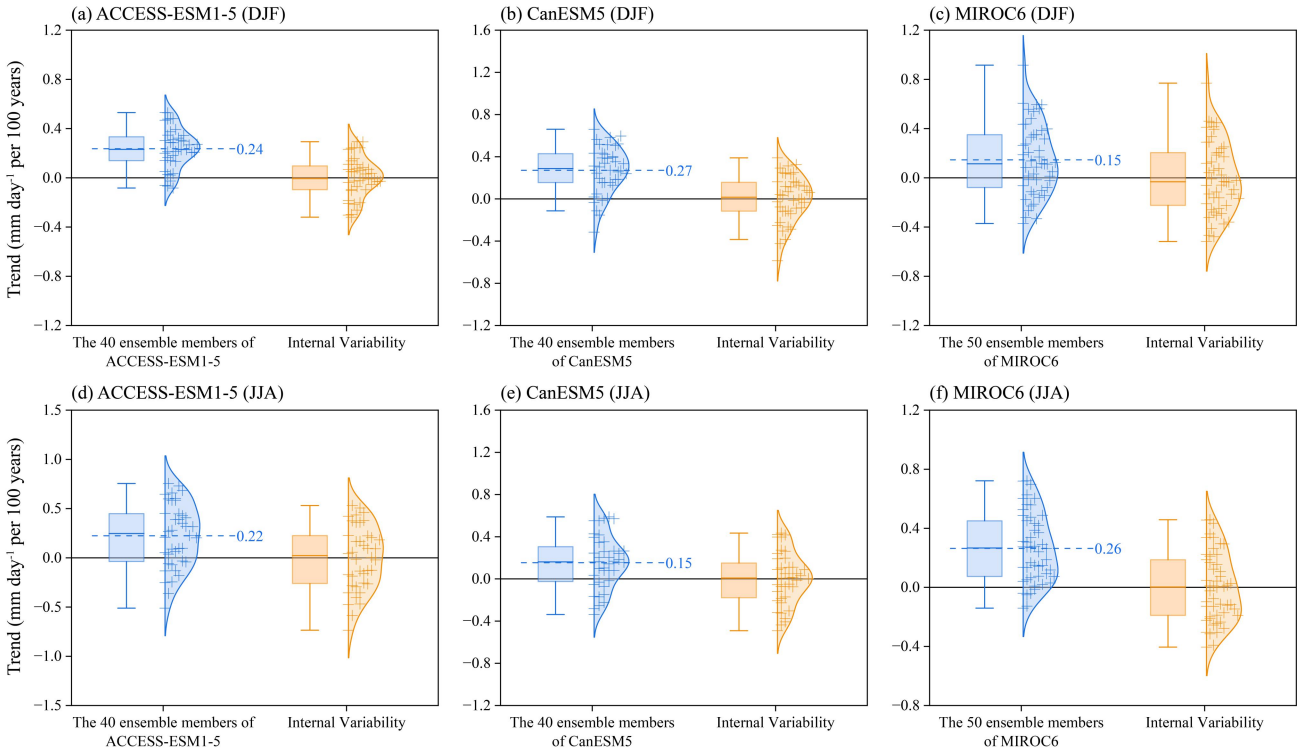

Figure S12. Linear trends (mm day^{-1} per 100 years) of precipitation during 1979–2014 from large ensembles of ACCESS-ESM1-5 (40 members), CanESM5 (40 members), and MIROC6 (50 members). (**a–c**) DJF precipitation trends. (**d–f**) JJA precipitation trends. The numbers and the dotted lines indicate the ensemble mean of the precipitation trends. Boxes indicate the 25th, 50th, and 75th percentiles and the whiskers indicate the minimum and maximum values. Plus signs represent the trends in regionally averaged precipitation from individual ensemble members, and curves show kernel density estimates of the trend distribution, with the bandwidth selected using Scott's rule.

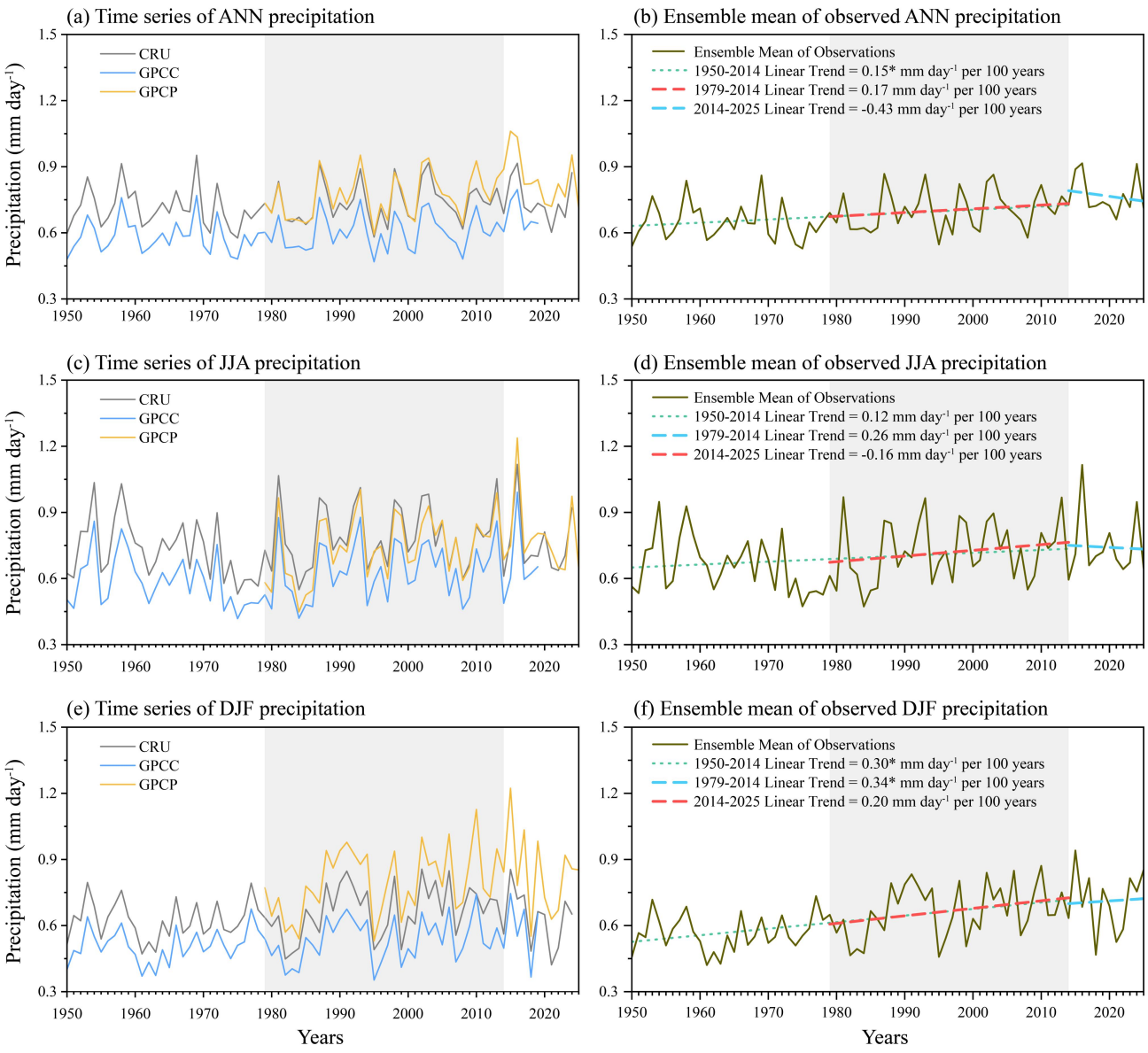

Figure S13. Time series of precipitation over Central Asia derived from GPCP (1979–2025), CRU (1950–2024), and GPCC (1950–2019). (**a**) Annual precipitation time series from the three observational datasets. (**b**) Annual precipitation time series of the ensemble mean of the three datasets. (**c, d**) Same as (**a, b**), but for winter precipitation. (**e, f**) Same as (**a, b**), but for summer precipitation. The dashed lines represent the liner trend in precipitation (mm day^{-1} per 100 years).

References

Myhre, G., Forster, P. M., Samset, B. H., Hodnebrog, Ø., Sillmann, J., Aalbergsjø, S. G., Andrews, T., Boucher, O., Faluvegi, G., Fläschner, D., Kasoar, M., Kharin, V., Kirkevåg, A., Lamarque, J.-F., Olivié, D., Richardson, T. B., Shindell, D., Shine, K. P., Stjern, C. W., Takemura, T., Voulgarakis, A., and Zwiers, F.: PDRMIP: A precipitation driver and response model intercomparison project—Protocol and preliminary results, Bull. Am. Meteorol. Soc., 98, 1185–1198, https://doi.org/10.1175/BAMS-D-16-0019.1, 2017.

Seland, Ø., Bentsen, M., Olivié, D., Toniazzo, T., Gjermundsen, A., Graff, L. S., Debernard, J. B., Gupta, A. K., He, Y.-C., Kirkevåg, A., Schwinger, J., Tjiputra, J., Aas, K. S., Bethke, I., Fan, Y., Griesfeller, J., Grini, A., Guo, C., Ilicak, M., Karset, I. H. H., Landgren, O., Liakka, J., Moseid, K. O., Nummelin, A., Spensberger, C., Tang, H., Zhang, Z., Heinze, C., Iversen, T., and Schulz, M.: Overview of the Norwegian Earth System Model (NorESM2) and key climate response of CMIP6 DECK, historical, and scenario simulations, Geosci. Model Dev., 13, 6165–6200, https://doi.org/10.5194/gmd-13-6165-2020, 2020.